

Nozzle Design for Vacuum Aerosol Deposition of Nanostructured Coatings

by

Trent Lee Hoffman

A Thesis Presented in Partial Fulfillment
of the Requirements for the Degree
Master of Science

Approved July 2017 by the
Graduated Supervisory Committee:

Zachary Holman, Chair
Marcus Herrmann
Michael Kozicki

ARIZONA STATE UNIVERSITY

August 2017

ABSTRACT

Nanomaterials exhibit unique properties that are substantially different from their bulk counterparts. These unique properties have gained recognition and application for various fields and products including sensors, displays, photovoltaics, and energy storage devices. Aerosol Deposition (AD) is a relatively new method for depositing nanomaterials. AD utilizes a nozzle to accelerate the nanomaterial into a deposition chamber under near-vacuum conditions towards a substrate with which the nanomaterial collides and adheres. Traditional methods for designing nozzles at atmospheric conditions are not well suited for nozzle design for AD methods.

Computational Fluid Dynamics (CFD) software, ANSYS Fluent, is utilized to simulate two-phase flows consisting of a carrier gas (Helium) and silicon nanoparticles. The Cunningham Correction Factor is used to account for non-continuous effects at the relatively low pressures utilized in AD.

The nozzle, referred to herein as a boundary layer compensation (BLC) nozzle, comprises an area-ratio which is larger than traditionally designed nozzles to compensate for the thick boundary layer which forms within the viscosity-affected carrier gas flow. As a result, nanoparticles impact the substrate at velocities up to 300 times faster than the baseline nozzle.

DEDICATION

For my wife, Kelsey, who has supported and inspired me in innumerable ways.

ACKNOWLEDGMENTS

It is my great pleasure to express my extreme sincere gratitude to my research advisor Dr. Zak Holman, without which this work would not have been possible. For his support, knowledge, and guidance, I am truly grateful.

I am greatly appreciative to my thesis committee, to Dr. Marcus Herrmann for his invaluable knowledge in computational fluid dynamics and for his willingness to review, critique and guide my work, and to Dr. Michael Kozicki for his willingness to review my work.

I would like to express my sincere appreciation to Ph.D. student, entrepreneur, and expert on nanoparticle deposition and coatings, Peter Firth, for his guidance and help validating computational results with real-world nanoparticle deposition.

Thanks to my parents for their never-ending love and support. To all of my brothers for their examples, with a special thanks to Justin for his time explaining CFD and JT for his time explaining thermal spray deposition. To my sisters for inspiring me to be a better man.

And most importantly of all, I would like to express my heartfelt thanks to my wife, Kelsey, for providing me with unfailing support and continuous encouragement throughout my years of study and through the process of researching and writing this thesis, and to our newborn son, Porter, for reminding me of the important things in life.

TABLE OF CONTENTS

	Page
LIST OF FIGURES	vi
LIST OF TABLES	viii
CHAPTER	
1 INTRODUCTION	1
1.1 Motivation	1
1.2 Overview of This Work.....	2
2 THERMAL SPRAY DEPOSITION METHODS	4
2.1 Cold Spray	4
2.2 Aerosol Deposition.....	5
2.3 Non-thermal Plasma Nanoparticles Synthesis	8
3 OVERVIEW OF SOLVER	12
3.1 ANSYS Fluent.....	12
3.2 Navier-Stokes Equations	12
3.3 Design Modeler	14
3.4 Mesh.....	14
3.5 Density-Based Solution Method	15
3.6 Discretization	17
4 OVERVIEW OF EXPERIMENT	19
4.1 Deposition Machine “Deppy”	19
4.2 Nozzle Design Theory.....	20
4.2.1 Isentropic Flow of Ideal Gas Through Nozzles	20
4.2.2 Non-Inviscid Flow	23

CHAPTER	Page
4.2.3 Reynolds Number	24
4.3 Isentropic Flow Equations Deficiencies.....	25
4.4 Fluid Flow Theory and Draft Force Calculation of Nanoparticles	26
4.4.1 Knudsen Number	26
4.4.2 Molecular Mean Free Path.....	27
4.4.3 Cunningham Correction Factor.....	28
4.5 CFD Validation	29
4.6 Boundary Conditions.....	30
4.7 Baseline Nozzle.....	32
4.8 AMNR Nozzle.....	32
4.9 BLC Nozzle.....	33
5 RESULTS	35
5.1 Carrier Gas Behavior (10mm stand-off)	35
5.2 Carrier Gas Behavior (20mm stand-off)	37
5.3 Nanoparticle Behavior (10mm stand-off)	38
5.4 Nanoparticle Behavior (20mm stand-off)	40
6 FUTURE WORK	42
WORKS CITED	43

LIST OF FIGURES

Figure	Page
1. Cartoon Depiction of NCs with Long Surface Ligands [21]	2
2. Particle Velocity vs. Particle Diameter	5
3. NC Behavior with Cold Spray (Left) and Aerosol Deposition (Right)	6
4. Aerosol Deposition Schematic Overview [5]	7
5. Model of Ceramic Particle Densification Mechanism on AD [29]	8
6. Left: Plasma reactor, Top Right: Size-Tunable Nanocrystals, Bottom Right: TEM Image of Nanoparticles Synthesized from Non-Thermal Plasma Reactor [31]	9
7. Nanoparticle Impact Velocity Versus Nozzle Pressure Ratio [25].....	10
8. Finite Control Volume for Quasi-One Dimensional Flow [38].....	13
9. Baseline Nozzle using Design Modeler	14
10. Mesh for Baseline Nozzle Using Meshing Tool.....	15
11. Overview of Density-Based Solution Method.....	16
12. Mesh for Nozzle Made of Mesh Cells	17
13. Rectangular Cell.....	18
14. Arizona State University's Deposition System, Deppy [40].....	19
15. Isentropic Supersonic Nozzle Flow [38].....	22
16. Various Regions of Flow Having a Boundary Layer [43].....	23
17. AMNR Nozzle	26
18. Drag Law Setting in ANSYS Fluent.....	29
19. Nanoparticle Velocities for Baseline Nozzle with Inlet Pressure of 2 Torr and Deposition Chamber Pressure of 0.4 Torr.	30

Figure	Page
20. Nozzle Inlet (red), Walls (yellow), and Outlet (blue).....	31
21. Baseline Nozzle	32
22. AMNR Nozzle	33
23. BLC nozzle	34
24. Velocity Contour Plot, Left: Baseline Nozzle; Center: AMNR Nozzle; Right: BLC Nozzle	35
25. Carrier Gas Velocity Magnitude Along Centerline of Nozzle.....	35
26. Absolute Pressure.....	36
27. Velocity Contour Plot, Left: Baseline Nozzle; Center: AMNR Nozzle; Right: BLC Nozzle	37
28. Carrier Gas Velocity Magnitude Along Centerline of Nozzle.....	38
29. Particle Streamlines, Left: Baseline Nozzle; Center: AMNR Nozzle; Right: BLC Nozzle	38
30. NC Velocity Along Centerline of Nozzle	39
31. Particle Streamlines, Left: Baseline Nozzle; Center: AMNR Nozzle; Right: BLC Nozzle	40
32. NC Velocity Along Centerline of Nozzle.....	41

LIST OF TABLES

Table	Page
1. Boundary Conditions	31
2. Nozzle Exit Pressures (Absolute)	36
3. NC Impact Velocities.....	41

1 INTRODUCTION

1.1 Motivation

Nanocrystals (NCs), also referred to as nanoparticles, and thin films manufactured using NCs are gaining recognition and application for various fields and products including sensors, displays, photovoltaics, light-emitting diodes, field-effect transistors (FETs), and energy storage devices [1, 2, 3, 4, 5, 6, 7, 8]. In contrast their bulk counterparts, NCs have been investigated for their use in the aforementioned fields in light of their unique electronic and optical properties [9, 10, 11, 12, 13, 1]. These technologies, however, often require well-controlled NC organization, density, and film thickness to achieve optimal performance and efficiency. Techniques that enable such control and precision during thin film formation are critically important in the development of new NC-based materials.

Common methods used to fabricate these types of thin films include solution-based deposition including spin-coating, drop-casting, and dip-coating methods [14, 15, 16, 17, 18, 19]. However, these methods may suffer from limited control over packing density or particle organization on the surface [20, 21]. The efficiency of these types of electronic devices depends on electronic charge transport across the NC films. Various studies show that for solution-based deposition methods, long-chain organic capping ligands, typically acquired during the chemical synthesis or “growth” process of NCs, for example for CdX and PbX (X = S, Se, Te), cause a decrease in NC density resulting in decreased charge transport across the NCs [21, 10, 22]. For example, consider the figure below of a cartoon depiction of an arrangement of NCs having long surface ligands.

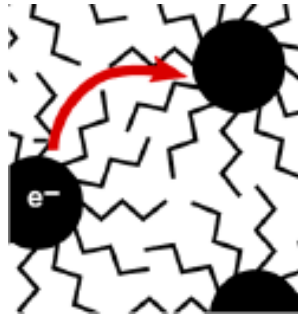


Figure 1 – Cartoon Depiction of NCs with Long Surface Ligands [21]

Increased energy is required for electronic charge transport across the low density NCs of the above figure.

Further methods include plasma spray and electrodeposition methods. However, plasma spray exposes particles to temperatures above their melting point whereby they may lose critical characteristics affiliated with NCs. Furthermore, electrodeposition is limited to conductive materials and suffers from low deposition rates.

Unlike plasma spray, cold spray deposition is a method in which the particles are not heated above their melting point [23]. However, as will be further described herein, cold spray deposition carries inherent characteristics which prevent NCs from being deposited using traditional cold spray methods.

1.2 Overview of This Work

This work will begin with an overview of nanomaterials and nanomaterial deposition methods. The primary focus will be on the design of the nozzle used to accelerate a carrier gas, which in turn accelerates the NCs, towards a substrate material. The work will examine the history of AD and introduce the deposition tool for which the nozzle is being designed.

The computational fluid dynamics (CFD) software, ANSYS Fluent, used to solve fluid flows through the deposition tool will be explored followed by an overview of traditional nozzle design methods. This will lead to the first set of results, conducted on the first iteration of the deposition tool's nozzle design. A second nozzle design for the tool is examined using traditional nozzle design equations which leads to the third and final nozzle design which takes into account viscous effects, namely boundary layers, of the carrier gas. Finally, the future of research and validation involving nozzle design for AD will be described.

2 THERMAL SPRAY DEPOSITION METHODS

Thermal spray is a generic term for a set of coating methods where a stream of particles is deposited on a substrate onto which the particles flatten and form essentially platelets, called splats, with several layers of these splats forming the coating. A bond forms between the particles and the substrate upon impact, with subsequent particles causing a build-up of the coating to its final thickness.

2.1 Cold Spray

Cold Spray is a type of thermal spray in which the temperatures to which the particles are exposed are contained below the melting point of the particles, hence the name “Cold” Spray [24]. A wide array of materials can be deposited in Cold Spray including metals, ceramics, composites, and polymers. Traditionally, cold spray is for micron-sized particles having diameters of between 5 and 100 micrometers. Cold Spray requires high upstream pressure (e.g., up to 700 psi or more) and typically employs downstream deposition chamber pressures of one atmosphere. However, Cold Spray methods are not ideal for NCs. The absolute pressure of the deposition process is an important factor in determining particle impact velocity [25]. As depicted in the figure below, the absolute pressures utilized in Cold Spray methods are ineffective for NCs.

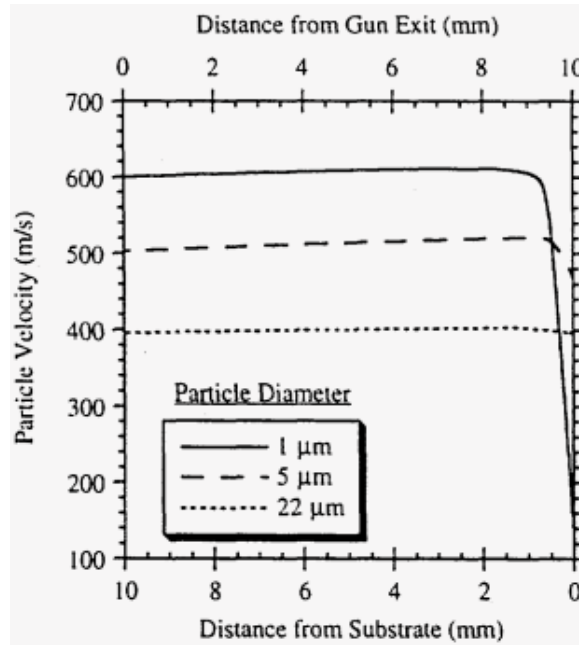


Figure 2 – Particle Velocity vs. Particle Diameter

As illustrated in Figure 1, the impact velocity of a particle decreases with the size of the particle with Cold Spray deposition. This is because the drag force of the carrier gas causes the smaller particles to follow the streamlines of the gas.

2.2 Aerosol Deposition

Aerosol Deposition (AD), also referred to as Vacuum Cold Spray (VCS) or Vacuum Kinetic Spraying (VKS) [26, 27] is a type of cold spray process adapted for deposition of NCs. However, instead of depositing particles at a deposition chamber pressure of around one atmosphere, the deposition chamber is held near vacuum (e.g., between .001 and 15 Torr). As a result of the lower absolute pressures employed in AD methods, the NCs do not follow the streamlines of the carrier gas flow as is found in higher pressure methods such as cold spray.

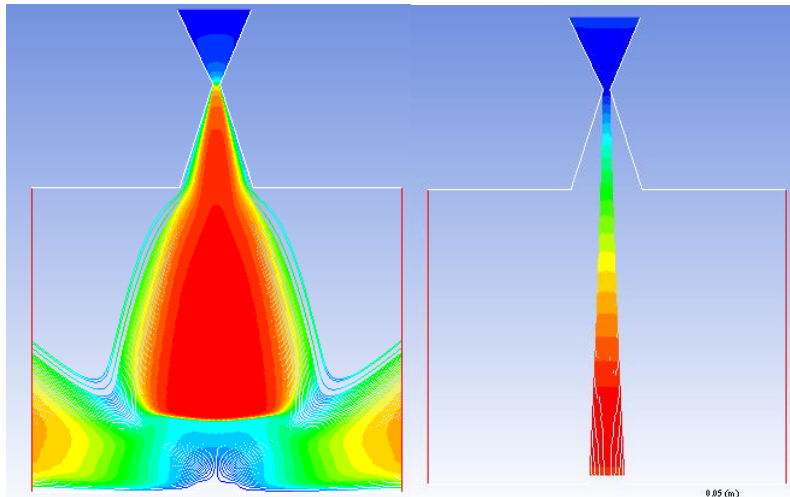


Figure 3 – NC Behavior with Cold Spray (left) and Aerosol Deposition (right)

The figure above illustrates the difference between NC behavior in Cold Spray (left) and AD (right). In cold spray, NCs will follow closely the streamlines of the carrier gas. Because the NCs follow the streamlines of the carrier gas so closely, they never impact the substrate. In AD, the NCs are less compliant towards the carrier gas flow because the density of the gas (near vacuum) is decreased compared to cold spray. In AD, the NCs are directed towards the substrate along a substantially linear flow path and contact the substrate. The major difference between Cold Spray and AD that allows the NCs to contact the substrate is the decreased deposition chamber pressure.

A common apparatus setup for AD is schematically illustrated in the below figure and utilizes an aerosol chamber for housing the particles. For aerosol generation, a carrier gas is passed through loose sub-micron sized powder contained in a vibrating chamber, thereby producing a fluidized bed. The aerosolized particles are carried from the aerosol chamber through a nozzle to the evacuated deposition chamber, accelerating through the nozzle to velocities of between 100 and 600 m/s [8], forming an aerosol jet at the nozzle's

outlet. The particles in the focused jet collide with the substrate at high speeds, bonding with the substrate to form the film.

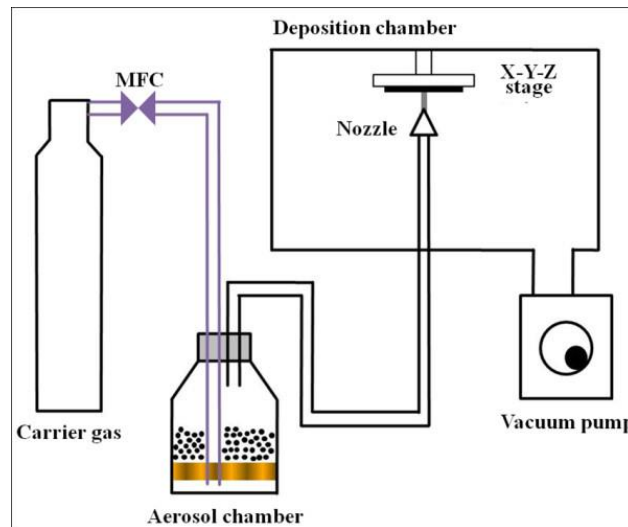


Figure 4 – Aerosol Deposition Schematic Overview [5]

One advantage to this system is the high density of thick films produced for ceramic materials, usually exceeding 95% of the theoretical material density [28]. The reason, in an experiment using particles of 20 nm in size or less at particle-substrate impact velocities of around 300 m/s, for high densities in these thick films (1-100 μ m thickness) has been explained to be a result of the fracturing of the brittle ceramic nanoparticles upon impaction with the substrate.

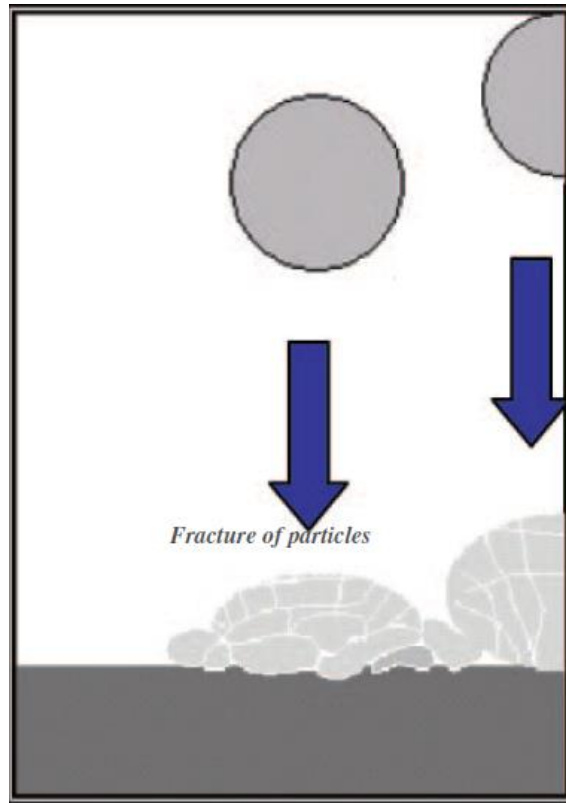


Figure 5 – Model of Ceramic Particle Densification Mechanism on AD [29]

However, this type of setup brings with it a number of disadvantages. Particles in the aerosol chamber may be strongly affected by agglomeration through Van-der-Waals interaction and electrostatic surface charge. Because of their high surface area and small size, the particles tend to form agglomerates and seldom exist as individual particles. This agglomeration can even be heightened when using vibration systems. Agglomerates can reduce deposition efficiency and coating quality [30, 8].

2.3 Non-thermal Plasma Nanoparticles Synthesis

In contrast to the aerosol chamber described above, one method to prevent particle agglomeration is the synthesis of nanoparticles in a non-thermal plasma. While a variety of nanoparticle materials have been explored, there is a particular interest in silicon

nanoparticles due to an already existing technological knowledge base for silicon-based materials.

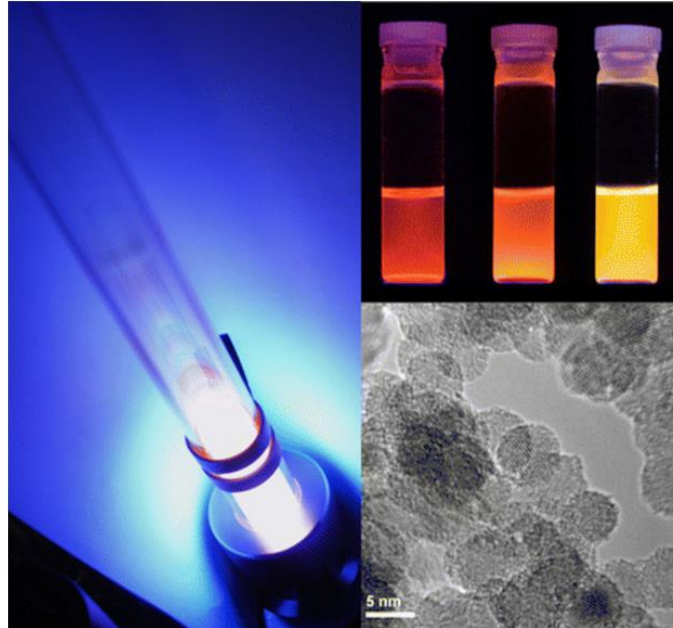


Figure 6 – Left: Plasma Reactor, Top Right: Size-Tunable Nanocrystals, Bottom Right: TEM Image of Nanoparticles Synthesized from Non-Thermal Plasma Reactor [31]

In general, non-thermal plasma nanoparticle synthesis utilized reactive precursor gasses, generally silane diluted in a carrier gas (He or Ar), introduced into the plasma chamber where the electrical discharge excites and dissociates the gas. By way of carrier collisions, a percentage of the dissociated precursor gas acquires enough energy for nucleation to occur. As the nucleated particles flow through the system they continue to grow with a final size proportional to the residence time in the chamber [32].

The synthesis of nanoparticles through non-thermal plasmas has become increasingly popular and exhibits unique features in terms of cleanliness and control of size and crystallinity [33, 32]. Furthermore, non-thermal plasma synthesis is inherently solvent and ligand-free, which enables the synthesis of nanocrystals with high purity [31].

Thin film deposition of silicon nanoparticles, however, is not without its drawbacks. Unlike brittle ceramics, it has proven difficult to deposit dense thin films for nanoparticles, such as silicon and germanium. In further contrast, silicon nanoparticles have shown a mechanical response from brittle to ductile when the nanoparticles' diameters decreased below a few hundred nanometers [34, 35, 36].

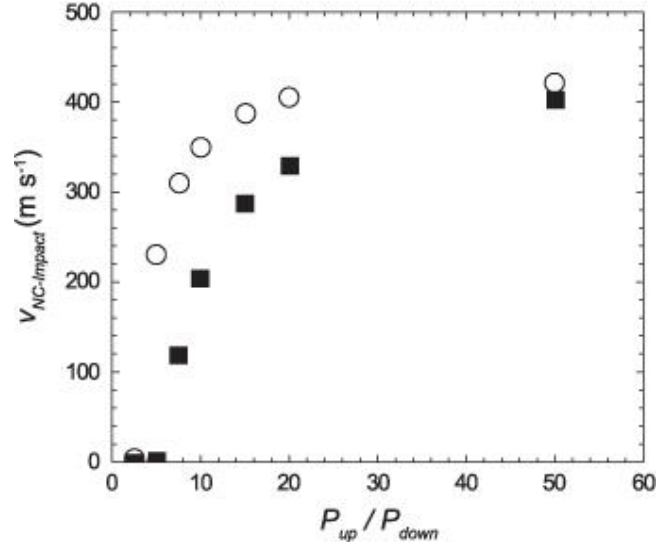


Figure 7 –Nanoparticle Impact Velocity Versus Nozzle Pressure Ratio [25]

One experiment provided maximum densities of around 56% of bulk density of non-thermal plasma-generated germanium nanoparticles deposited onto a silicon substrate [25]. In the experiment, the film density increased with increasing nanoparticle velocities. While porous films find use in certain applications, such as gas-sensing and catalysis for example, they are unsuitable for use in semiconductor devices in which charge carriers must pass between neighboring nanoparticles. Thus, there is a push for attaining higher film densities for silicon and germanium nanoparticles, such as the densities of ceramic films discussed earlier. As demonstrated in the experiment, it is probable that increasing the velocities of the nanoparticles will increase particle density. Thus, this work aims to

design a nozzle for aerosol deposition applications, in which the particles attain a higher impact velocity for a given pressure ratio.

3 OVERVIEW OF SOLVER

3.1 ANSYS Fluent

ANSYS Fluent (Fluent) is a computational fluid dynamics (CFD) fluid flow solver. Fluent provides comprehensive modeling capabilities for a wide range of compressible and incompressible, turbulent and laminar fluid flow problems. Steady-state or transient analysis can be performed. Another very useful model in Fluent is the multiphase flow model, such as the discrete phase model (DPM). Multiphase flows include gas-liquid, gas-solid, liquid-solid, and gas-liquid-solid flows. For all flows, Fluent solves conservation equations for mass and momentum [37]. For flows involving heat transfer or compressibility an additional equation for energy conservation is solved. These equations are often collectively referred to as the Navier-Stokes equations.

3.2 Navier-Stokes Equations

The governing equations for steady quasi-one-dimensional flow are obtained by applying the integral form of the conservation equations to the variable-area control volume, or nozzle, depicted in Figure 1 [38].

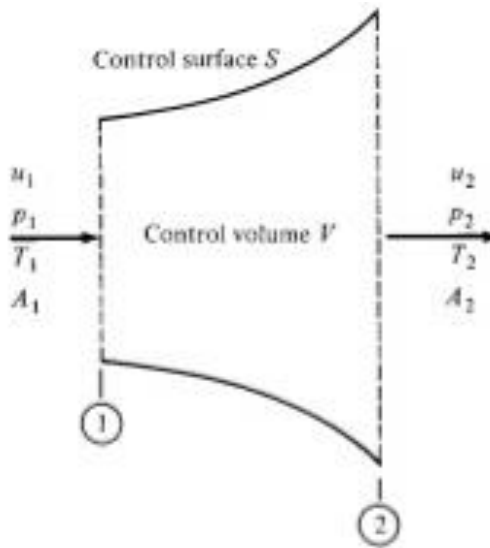


Figure 8 – Finite Control Volume for Quasi-One Dimensional Flow [38]

The integral form of the continuity equation is:

Equation 1

$$-\oint_S \rho \mathbf{V} \cdot d\mathbf{S} = \frac{\partial}{\partial t} \iiint_V \rho dV$$

When integrated over the control volume of Figure 1, the continuity equation becomes:

Equation 2

$$\rho_1 u_1 A_1 = \rho_2 u_2 A_2$$

Where:

ρ_x = density at location x

u_x = velocity at location x

A_x = area at location x

The integral form of the momentum equation is:

Equation 3

$$\oint_S (\rho \mathbf{V} \cdot d\mathbf{S}) \mathbf{V} + \iiint_V \frac{\partial(\rho \mathbf{V})}{\partial t} dV = \iiint_V \rho \mathbf{f} dV - \oint_S \rho d\mathbf{S}$$

When integrated over the control volume of Figure 1, the momentum equation becomes:

Equation 4

$$\rho_1 A_1 + \rho_1 u_1^2 A_1 + \int_{A_1}^{A_2} p dA = \rho_2 A_2 + \rho_2 u_2^2 A_2$$

The integral form of the energy equation is:

Equation 5

$$\begin{aligned} \iiint_V \dot{q} \rho dV - \oint_S \rho \mathbf{V} \cdot d\mathbf{S} + \iiint_V \rho (\mathbf{f} \cdot \mathbf{V}) dV \\ = \iiint_V \frac{\partial}{\partial t} \left[\rho \left(e + \frac{V^2}{2} \right) \right] dV + \oint_S \rho \left(e + \frac{V^2}{2} \right) \mathbf{V} \cdot d\mathbf{S} \end{aligned}$$

When integrated over the control volume of Figure 1 the energy equation becomes:

Equation 6

$$h_1 + \frac{u_1^2}{2} = h_2 + \frac{u_2^2}{2}$$

Where:

h_x = enthalpy at location x

The energy equation states that the total enthalpy is constant along a streamline of a flow [38].

3.3 Design Modeler

Before the solver parameters are set, the first step taken using ANSYS Fluent is to generate a model of the nozzle and the deposition chamber using Design Modeler in ANSYS. The figure below illustrates the baseline nozzle, as will be introduced herein with a substrate at a 10mm stand-off distance.

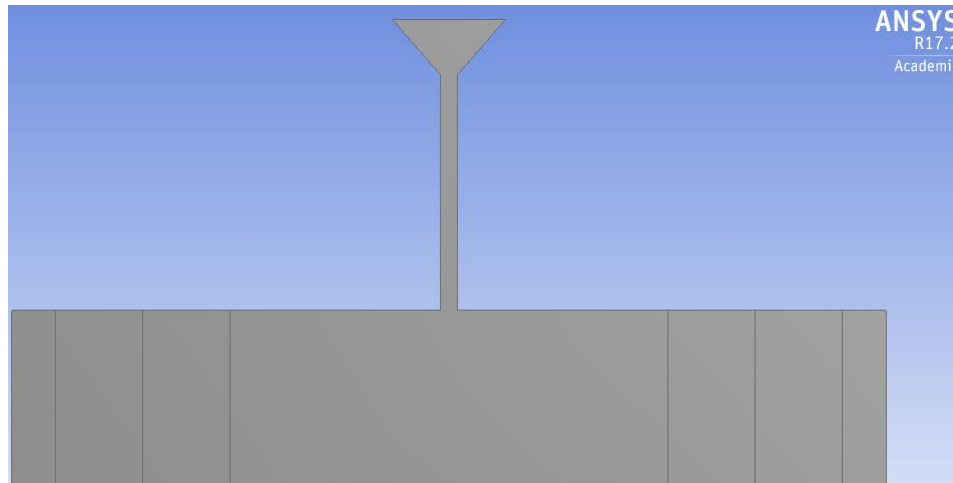


Figure 9 – Baseline Nozzle Using Design Modeler

3.4 Mesh

After designing the nozzle in the Design Modeler, the Meshing tool is used to generate a mesh. The minimum mesh element size in the nozzle and between the nozzle exit and the substrate was defined as 50 micrometers. The cell size increases towards the

far-field area near the deposition chamber exits. A grid refinement was performed to ensure grid independence.

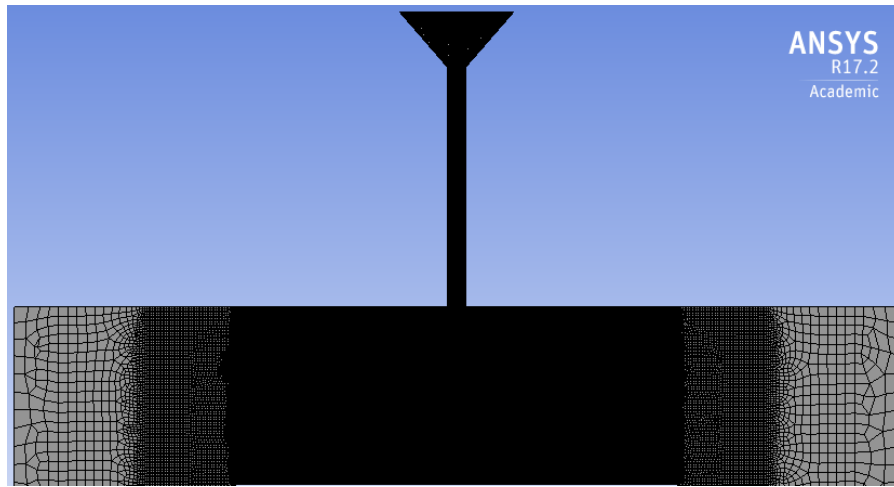


Figure 10 – Mesh for Baseline Nozzle Using Meshing Tool

3.5 Density-Based Solution Method

ANSYS Fluent includes two solvers: pressure-based and density-based. Historically speaking, the pressure-based approach was developed for low-speed incompressible flows, while the density-based approach was mainly used for high-speed compressible flows. However, recently both methods have been extended and reformulated to solve and operate for a wide range of flow conditions beyond their traditional or original intent. Because the pressure-based solver traditionally has been used for incompressible and mildly compressible flows, the density-based solver was chosen as the solver for the trials described in this paper.

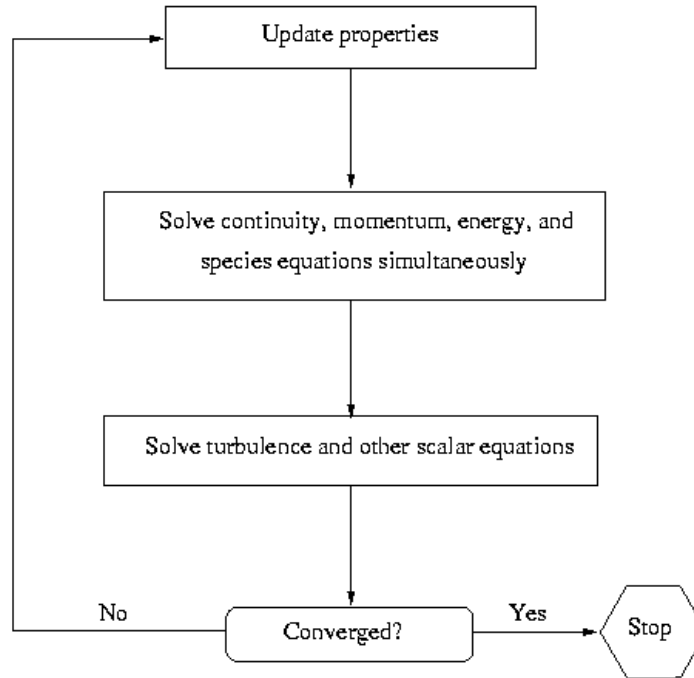


Figure 11 – Overview of Density-Based Solution Method

As illustrated in Figure 4, the density-based solver works by solving the coupled system of equations (continuity, momentum, energy, and species equations if available). Where appropriate, equations for scalars such as turbulence and other scalar equations are solved. Then, convergence of the equations set is checked and the process continues until the convergence criteria are met.

3.6 Discretization

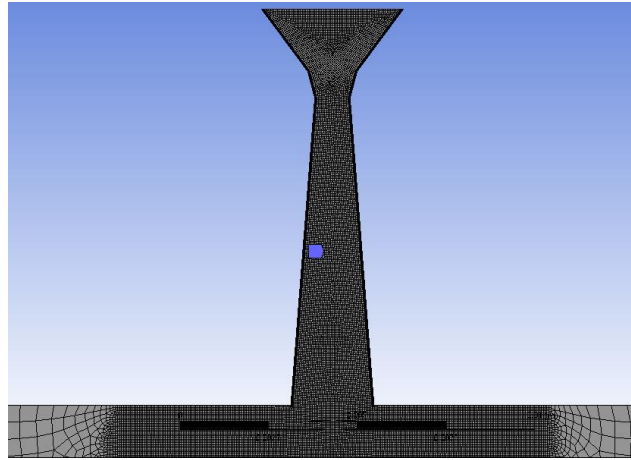


Figure 12 – Mesh for Nozzle Made of Mesh Cells

With reference to the figure above, it is shown that a mesh consists of quadrilaterals. Fluent uses the finite-volume method to solve the Navier-Stokes equations. The integral form of the Navier-Stokes equations are applied to the control volume defined by a cell to get the discrete equation for the cell. For example, the integral form of the continuity equation for steady, incompressible flow is [39]:

Equation 7

$$\int_S \vec{V} \cdot \hat{n} dS = 0$$

Where:

S = surface of the control volume

\hat{n} = outward normal at the surface

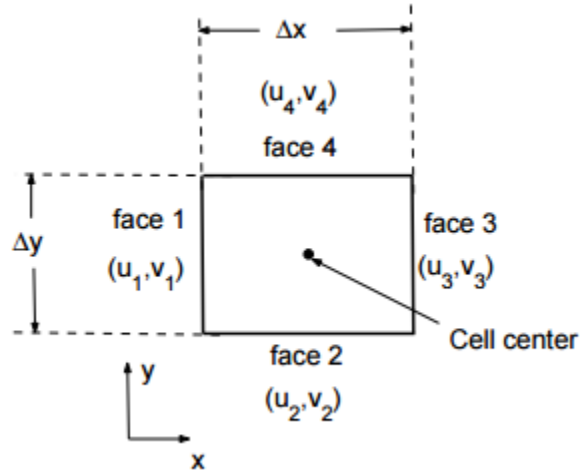


Figure 13 – Rectangular Cell

Consider the rectangular cell shown in figure 5. The velocity at face i can be written as $\vec{V}_i = u_i\hat{i} + v_j\hat{j}$. Now, applying the mass conservation equation to the cell-defined control volume gives [39]:

Equation 8

$$-u_1\Delta y - v_2\Delta x + u_3\Delta y + v_4\Delta x = 0$$

The above equation gives the discrete form of the continuity equation for the cell illustrated in Figure 9. It is equivalent to setting the sum of the net mass flow into the control volume equal to zero, thereby ensuring that mass is conserved for the cell.

4 OVERVIEW OF EXPERIMENT

4.1 Deposition Machine “Deppy”

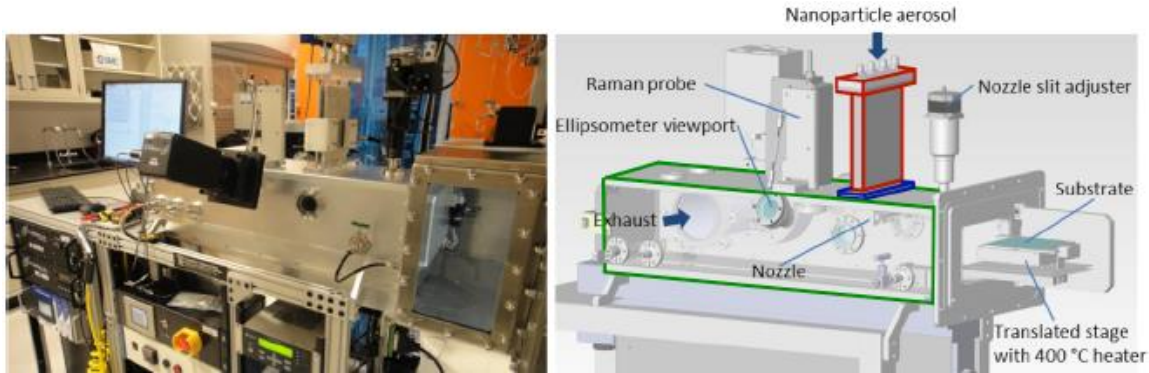


Figure 14 - Arizona State University's Deposition System, Deppy [40]

Deppy comprises three primary sections shown in Figure 7, the reaction chamber (red), the nozzle (blue) and the deposition chamber (green). Precursor gasses are introduced to the reaction chamber where the nanoparticles are formed/modified. The details of the chemistry that occurs in the reaction chamber is material specific. For this reason, Deppy’s reaction chamber was designed to be easily and inexpensively removed and replaced to fit the specific application [40].

After passing through the reaction chamber, the nanoparticles are accelerated through the nozzle and into the deposition chamber where they impact a substrate that passes beneath the jet stream, forming a uniform film of nanoparticles. The velocity of the nanoparticles upon impaction is dependent on the reaction chamber and deposition chamber pressure ratio and the nozzle geometry. The experiments described herein set out to design a new nozzle for Deppy which increases that velocity of nanoparticles for a given pressure ratio.

4.2 Nozzle Design Theory

A nozzle is a device for controlling specific characteristics of a fluid (gas or liquid) flowing through it. As the fluid passes from the inlet to the exit of the nozzle, the thermal energy of the fluid is converted to kinetic energy, so the velocity of the fluid is increased [41]. Nozzles can be circular, rectangular, square, or oval. This work deals only with rectangular section nozzles having a slit-shaped orifice. Accordingly, a rectangular nozzle may have a high aspect-ratio outlet suitable for depositing thin films of NCs over a large surface area.

4.2.1 Isentropic Flow of Ideal Gas Through Nozzles

For De-Laval nozzles under supersonic conditions, the area ratio of the nozzle and the Mach number of the flow at any given location within the nozzle are related. Pressure and temperature are also related to the Mach number. The *area-Mach number relation* is provided in the below equation [38]:

Equation 9

$$\left(\frac{A}{A^*}\right)^2 = \frac{1}{M^2} \left[\frac{2}{\gamma + 1} \left(1 + \frac{\gamma - 1}{2} M^2 \right) \right]^{(\gamma+1)/(\gamma-1)}$$

Where:

A = nozzle area at a specified location (x)

A^* = nozzle area at the throat

M = Mach number of the gas at the specified location (x)

γ = specific heat of the gas

The *pressure-Mach number relation* is provided in the below equation [38]:

Equation 10

$$\frac{p}{p_0} = \left(1 + \frac{\gamma - 1}{2} M^2 \right)^{(-\gamma)/(\gamma-1)}$$

Where:

p = gas pressure at a specified location (x)

p_0 = gas inlet pressure

The *temperature-Mach number relation* is provided in the below equation [38]:

Equation 11

$$\frac{T}{T_0} = \left(1 + \frac{\gamma - 1}{2} M^2\right)^{-1}$$

Where:

T = gas temperature at a specified location (x)

T_0 = gas inlet temperature

The Figure depicted below illustrates pressure ratio and temperature ratio of air versus position (x) through a De Laval nozzle, according to equations 10 and 11 above.

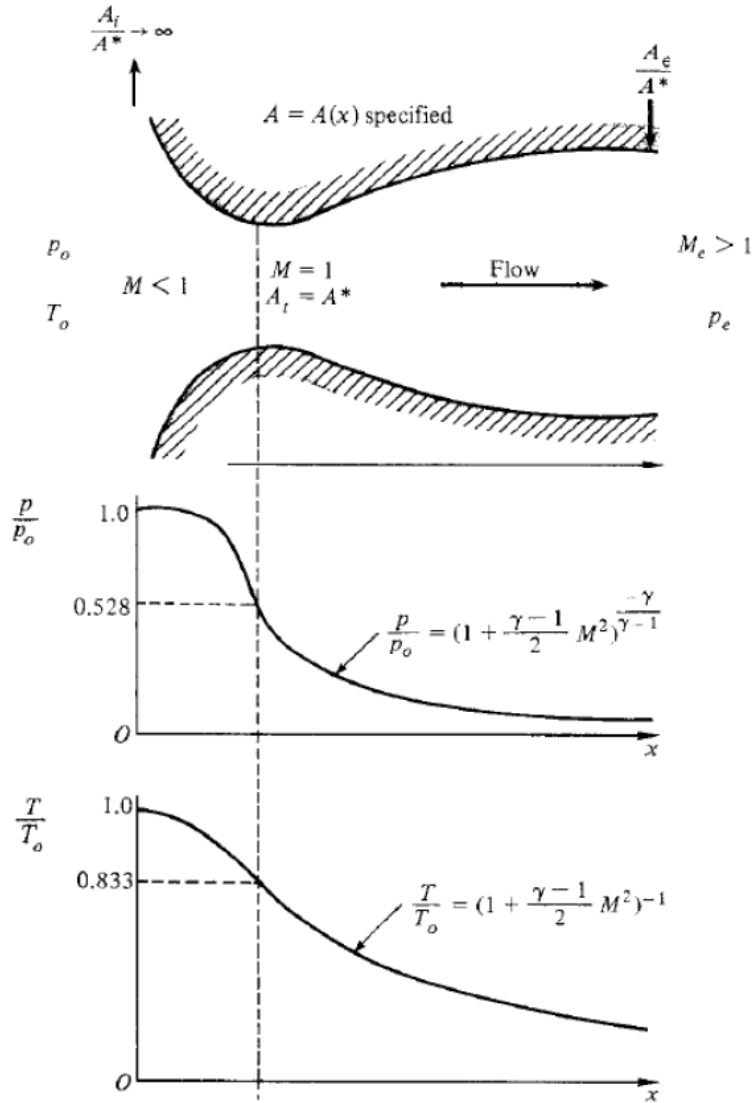


Figure 15 – Isentropic Supersonic Nozzle Flow [38]

If the pressure ratio across the nozzle is known, then from the above isentropic flow equations, there is only one unique area ratio for which supersonic flow will be isentropic. Under isentropic flow conditions, the back pressure (i.e., the atmospheric pressure or chamber pressure downstream from the nozzle exit plane) is equal to the nozzle exit pressure. If the nozzle exit pressure has expanded below the back pressure, the nozzle is said to be *overexpanded* and a shock may form in the diverging section of the nozzle.

Conversely, if the nozzle exit pressure is greater than the back pressure, the nozzle is said to be *underexpanded* and hence the flow is capable of additional expansion after leaving the nozzle.

4.2.2 Non-Inviscid Flow

A quanta of data is available with regard to nozzle design for inviscid flows [41] - [42]. The breaking point for this type of design is, however, when flows are no longer inviscid. For an inviscid fluid there are no shearing stresses [43]. That is to say that the fluid's weight and pressure forces are the only forces acting on the fluid. For truly inviscid flow with no shearing stress, the flow would merely "slip" along the flow surface. Under real conditions however, the flow velocity changes from zero at the boundary (no-slip condition) to a relatively large velocity forming a boundary layer at the wall of the flow surface as depicted below.

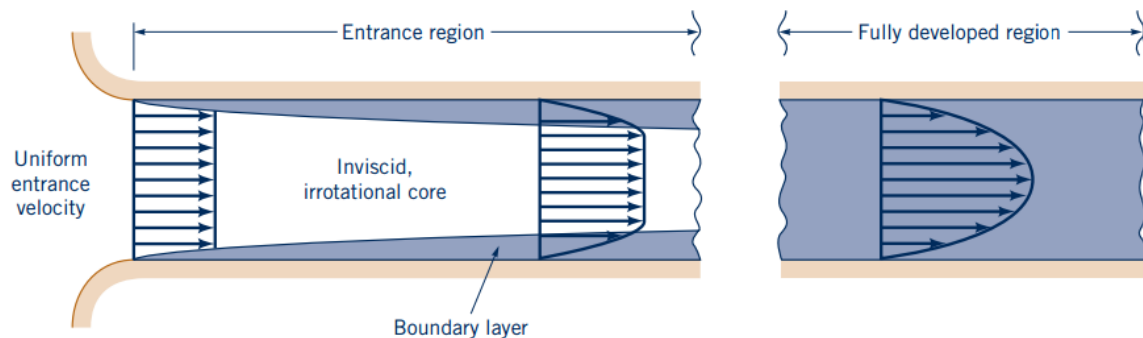


Figure 16 – Various Regions of Flow Having a Boundary Layer [43]

It becomes clear from the figure above that the boundary layer becomes particularly relevant for flows through a conduit or nozzle because the flow is surrounded by a surface. This relevancy increases as the Reynolds number of the flow decreases. As depicted, the boundary layer matures from the entrance region to the fully developed region such that the velocity profile is parabolic.

To illustrate the problems with the *area-Mach number relation* for non-inviscid flows, consider the following.

4.2.3 Reynolds Number

One indicator of the relative viscosity, or boundary layer thickness, of a flow is the Reynolds number. As an object moves through a gas, or stated in reverse, if a gas moves around an object, the gas molecules near the object are disturbed and move around the object. Aerodynamic forces are generated between the gas and the object. The magnitude of these force depend on [44]:

- The shape of the object
- The speed of the object
- The mass of the gas going by the object
- The viscosity of the gas
- The compressibility of the gas

The Reynolds number (Re) is a dimensionless ratio of the inertial (resistant to change or motion) forces to viscous (heavy and gluey) forces. Reynolds number can be defined as [44]:

Equation 12

$$Re = \frac{\text{Inertia Force}}{\text{Viscous Force}} = \frac{V L}{\nu}$$

Where:

V = velocity of fluid with respect to flow surface

L = characteristic linear dimension

ν = kinematic viscosity

From the above equation it can be seen that the Reynolds number is inversely proportional to the viscosity of the fluid. High Reynolds number values (on the order of 10

million) indicate that viscous forces are small and the flow is essentially inviscid. Low values of Reynolds number (on the order of 100) indicate that viscous forces must be considered [44]. Thus, the lower the Reynolds number the weaker the inviscid assumption of chapter 4.2.1 becomes.

4.3 Isentropic Flow Equations Deficiencies

As previously mentioned, the *area-Mach number relation* is often used in designing a nozzle area ratio. A recent study reports increased particle velocity for a nozzle designed using the *area-Mach number relation* for determining the area ratio of the nozzle [41]. However, in the study, the design is for flows at or above atmospheric pressure. For the low pressures utilized for nanoparticles in AD, it was discovered in this experiment that the *area-Mach number relation* is no longer valid. This invalidity arises because viscous effects begin to dominate the flow for AD methods. The figure below illustrates a contour plot of velocity magnitude for a nozzle designed using the *area-Mach number relation* (AMNR Nozzle) for AD conditions.

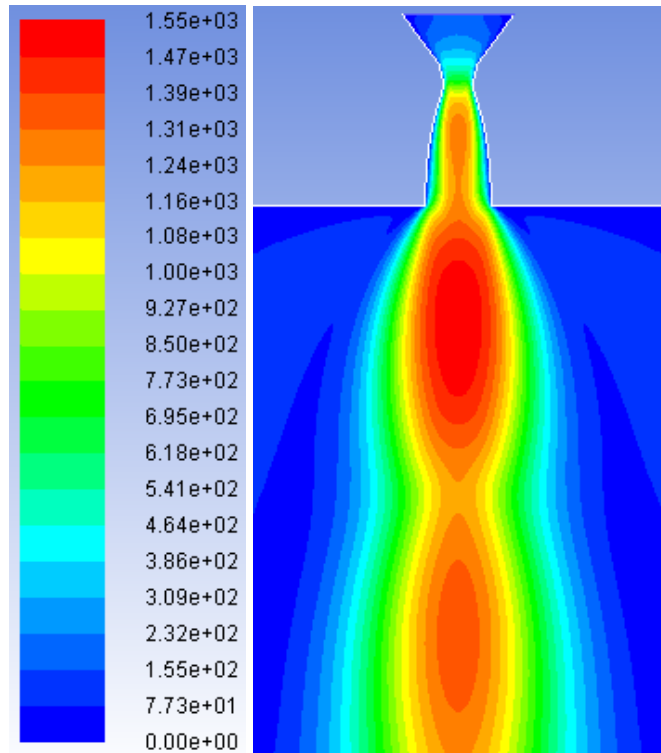


Figure 17 - AMNR Nozzle

The above figure illustrates the AMNR nozzle which is under-expanded due to the boundary layer not being taken into account when designing the nozzle under inviscid assumption. As can be seen in the figure, the fluid continues expanding after it leaves the exit plane of the nozzle. Thus, a new method is necessary for nozzles used for AD.

4.4 Fluid Flow Theory and Draft Force Calculation of Nanoparticles

4.4.1 Knudsen Number

The Knudsen number Kn is usually defined for a gas as the ratio $Kn = \lambda/L$ where λ is the mean free path and L is any macroscopic dimension of interest. The importance of this number is that, when $Kn \ll 1$, the gas behaves as a continuum fluid on the length scale L . The regime in which $Kn \ll 1$ is known as the hydrodynamic regime while that in which $Kn \gg 1$ is known as the Knudsen regime. In the former, the gas obeys the Navier-stokes

equations of hydrodynamics (which is what Ansys Fluent assumes) while the latter, rarefied gas dynamics apply.

- Continuum Flow ($Kn < 0.01$)
- Slip Flow ($0.01 < Kn < 0.1$)
- Transitional Flow ($0.1 < Kn < 10$)
- Free molecular flow ($Kn > 10$)

4.4.2 Molecular Mean Free Path

The mean free path, or average distance between collisions for a gas molecule, may be estimated from kinetic theory and ideal gas law which lead to equation 13 as follows [45]:

Equation 13 - Mean Free Path

$$\lambda = \frac{RT}{\sqrt{2}\pi d^2 N_A P}$$

Where:

R = Universal gas constant

T = Temperature

d = Molecule Diameter

N_A = Avogadro's Number

P = Absolute Pressure

In the experiments discussed herein the deposition chamber pressure may be relatively low (e.g., pressures around 1 Torr). Such low pressures indicate fewer molecular collisions and decreased compliance with the Navier-Stokes equations. Stated differently, the low pressures of AD methods force transitional, or free molecular flow, where the accuracy of the Navier-Stokes equations are decreased. There are, however, methods for compensating for non-continuum effects.

4.4.3 Cunningham Correction Factor

In fluid dynamics, the Cunningham correction factor, or Cunningham slip correction factor, is used to account for non-continuum effects when calculating the drag on small particles. The derivation of Stokes Law, which is used to calculate the drag force on small particles, assumes a no-slip condition which is no longer correct at high Knudsen numbers. The Cunningham slip correction factor allows predicting the drag force on a particle moving a fluid with Knudsen number between the continuum regime and free molecular flow.

For sub-micron particles, a form of Stoke's draw law is available in Ansys Fluent to calculate the draft force (F_D) on the sub-micron particle using the following equation [37]:

Equation 14 - Sub-micron Drag Force

$$F_D = \frac{18\mu}{d_p^2 \rho_p C_c}$$

Where:

ρ_p = Particle Density

μ = Molecular viscosity of the fluid

The Cunningham Correction Factor (C_c) is calculated using equation 15 as follows [37]:

Equation 15 - Cunningham Correction Factor

$$C_c = 1 + \frac{2\lambda}{d_p} (1.257 + 0.4e^{-(1.1d_p/2\lambda)})$$

Where:

λ = Molecular mean free path

d_p = Particle Diameter

The Cunningham Correction Factor is activated in ANSYS Fluent according to equation 13 to account for anticipated non-continuum errors in the carrier fluid flow field. The figure below illustrates the Cunningham Correction Factor setting in the Discrete Phase model settings of Fluent. For a reaction chamber pressure of 1 Torr, a carrier gas comprising Helium, and 5nm particles, the Cunningham Correction Factor is calculated to be 436,930.

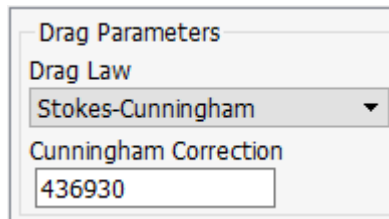


Figure 18 – Drag Law setting in ANSYS Fluent

4.5 CFD Validation

Before performing computational calculations on a new nozzle design, ANSYS Fluent was validated by running trials using the existing nozzle geometry and boundary conditions for known thin film deposits. The trial was for a pressure ratio of 5 with a nozzle inlet pressure of 2 torr and a deposition chamber pressure of 0.4 torr. From pre-deposited silicon nanoparticle films it was expected that the particle velocity would be greater at a stand-off distance of 10mm than a stand-off distance of 20mm. The figure below provides velocities for particles located along the centerline of the baseline nozzle. The nozzle outlet is located at distance “0” along the x-axis.

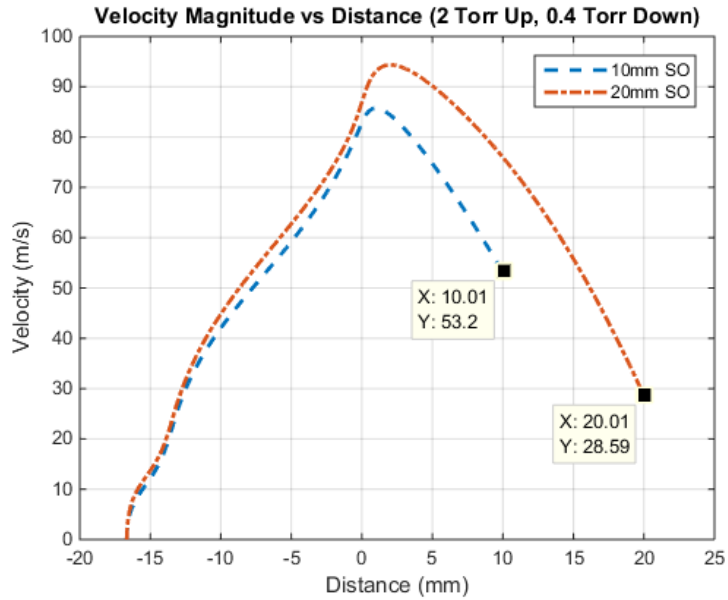


Figure 19 – Nanoparticle Velocities for Baseline Nozzle with Inlet Pressure of 2 Torr and Deposition Chamber Pressure of 0.4 Torr.

The results given by ANSYS Fluent were qualitatively consistent with the expected results provided the known film densities deposited using Deppy under identical conditions.

4.6 Boundary Conditions

Figure 8 illustrates the grid for a nozzle and deposition chamber illustrating where the inlet (red), walls (yellow), and outlet (blue) of the grid are defined.

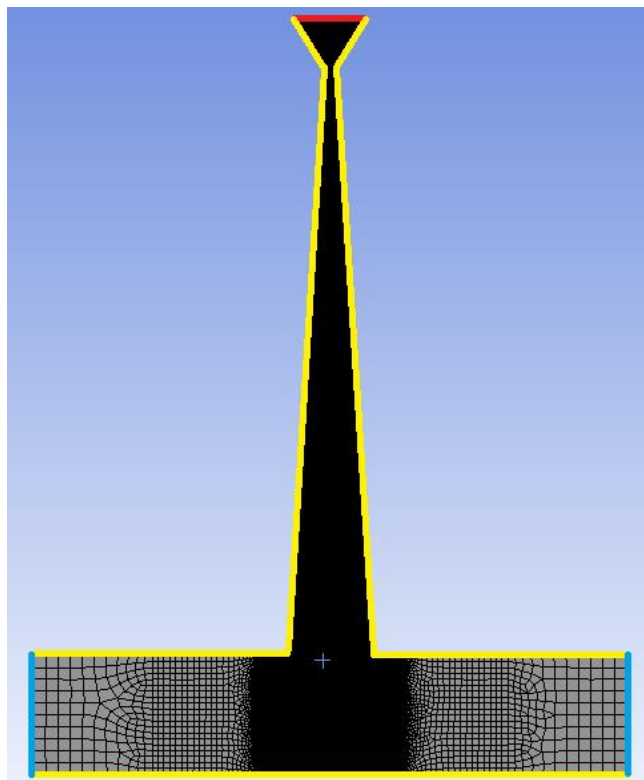


Figure 20 - Nozzle Inlet (red), Walls (yellow), and Outlet (blue)

The boundary conditions are provided in table 1 below.

Table 1 – Boundary Conditions

Inlet Pressure	20 Torr (2666.45 Pa)
Outlet Pressure	1 Torr (133.32 Pa)

The Carrier gas was chosen as Helium (He) and the nanoparticles were chosen to be silicon nanoparticles with a diameter of 5 nanometers (5 nm). The walls were defined with the no-slip condition to accurately model inviscid flow. Namely, the carrier gas velocity is defined as zero at the walls.

4.7 Baseline Nozzle

The nozzle being used as a baseline is illustrated in the figure below. The baseline nozzle is the original nozzle used in Deppy. The nozzle was chosen as a baseline because real data for the nozzle was readily available to validate CFD results.

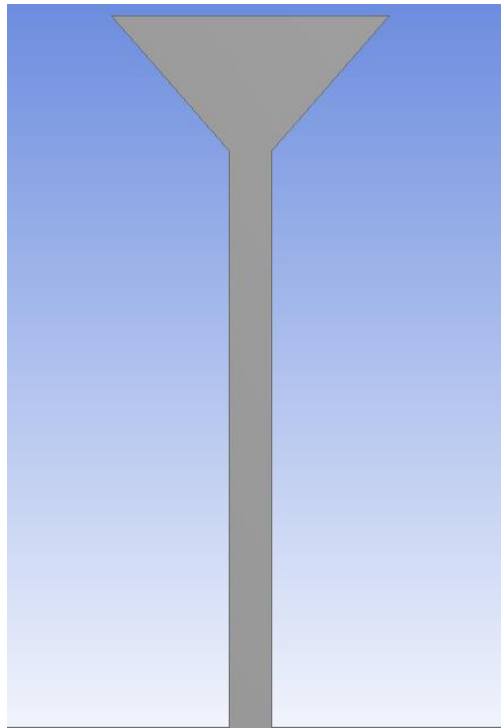


Figure 21 - Baseline Nozzle

The baseline nozzle simply consists of a converging section and an extended “throat” section comprising a constant cross-sectional area. The throat section has a width of 1mm.

4.8 AMNR Nozzle

The AMNR nozzle is designed by first solving the *pressure-Mach number relation* for a given pressure ratio. The pressure ratio ($\frac{p}{p_0}$) used in this experiment is .05 which would give an exit Mach number of 2.6348. This Mach number is then used to solve for the area

ratio $\left(\frac{A}{A^*}\right)$ using the *area-Mach number relation*. Setting the Mach number to 2.6348 in the *area-Mach number relation* gives an area ratio $\left(\frac{A}{A^*}\right)$ of 2.3556.

The figure below illustrates the AMNR Nozzle per the design described above.

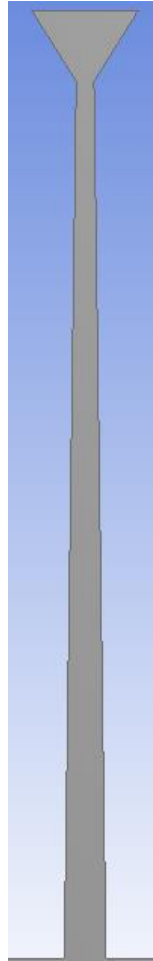


Figure 22 - AMNR Nozzle

4.9 BLC Nozzle

The BLC nozzle is similar to the AMNR nozzle except that the area ratio is increased to 7.0 to compensate for the boundary layers formed near the walls of the nozzle. The area ratio was chosen experimentally in order to match the nozzle exit plane pressure with the deposition chamber pressure.

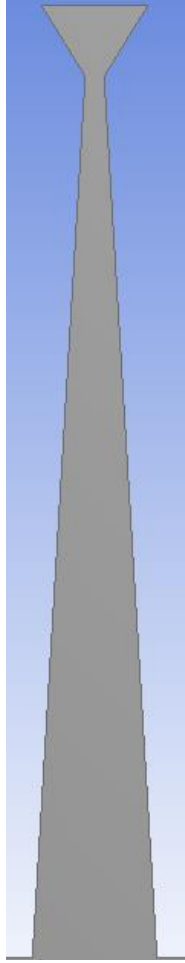


Figure 23 - BLC Nozzle

5 RESULTS

The Experiments that follow had two goals.

- 1) Increase carrier gas velocity for a given pressure ratio
- 2) Numerically calculate velocity of nanoparticles introduced into the carrier gas

5.1 Carrier Gas Behavior (10mm stand-off)

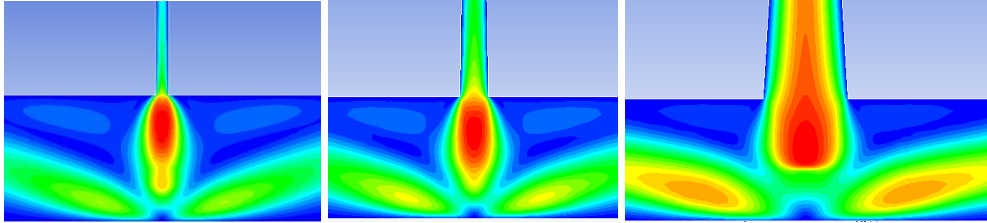


Figure 24 – Velocity Contour Plot, left: Baseline Nozzle; center: AMNR Nozzle; right: BLC Nozzle

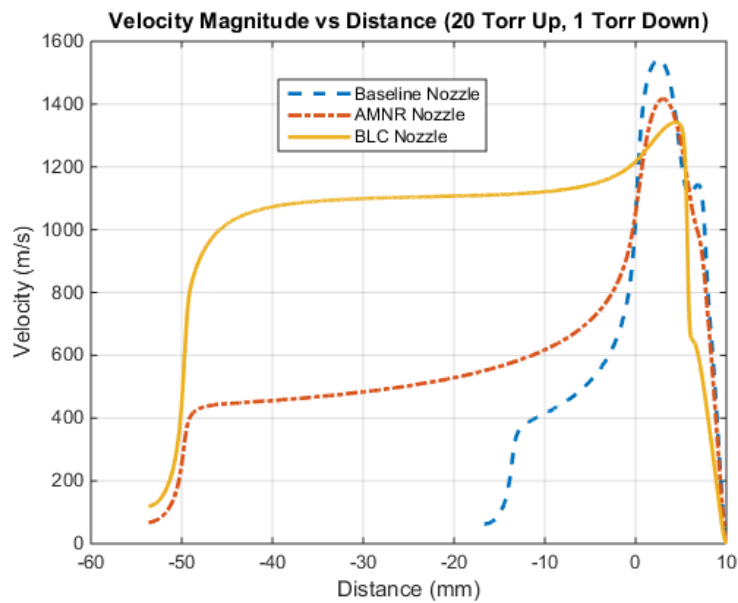


Figure 25 – Carrier Gas Velocity Magnitude Along Centerline of Nozzle

Although the maximum velocity magnitude aft of the exit plane (0 mm) of the BLC nozzle is minimized when compared to the baseline nozzle and the AMNR nozzle, the carrier gas velocity is much greater within the BLC nozzle than the other two nozzles. This

proves to be advantageous for accelerating the NCs prior to exiting the nozzle, as will be seen in the sections that follow.

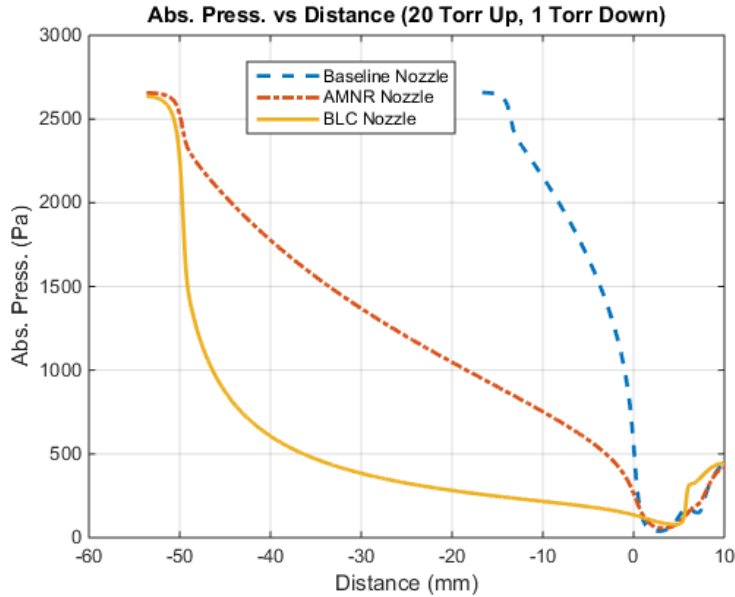


Figure 26 – Absolute Pressure

The above figure illustrates the absolute pressure of the nozzles. While much of the expansion occurs at the nozzle exit for the baseline and the AMNR nozzle, almost all of the expansion occurs in the nozzle for the BLC nozzle. Table 2 below provides the nozzle exit pressures for each of the nozzles. The nozzle exit pressure for the baseline nozzle is well over the deposition chamber pressure of 133.332 Pa and the nozzle exit pressure for the AMNR nozzle is also above the deposition chamber pressure, although not as severely under-expanded as the baseline nozzle. The nozzle exit pressure for the BLC nozzle is just slightly above the deposition chamber pressure, indicating that the nozzle is almost properly expanded and just slightly under-expanded.

Table 2 – Nozzle Exit Pressures (Absolute)

Nozzle Type	Nozzle Exit Pressure (Pa)
-------------	---------------------------

Baseline	560
AMNR	265
BLC	135.6

5.2 Carrier Gas Behavior (20mm stand-off)

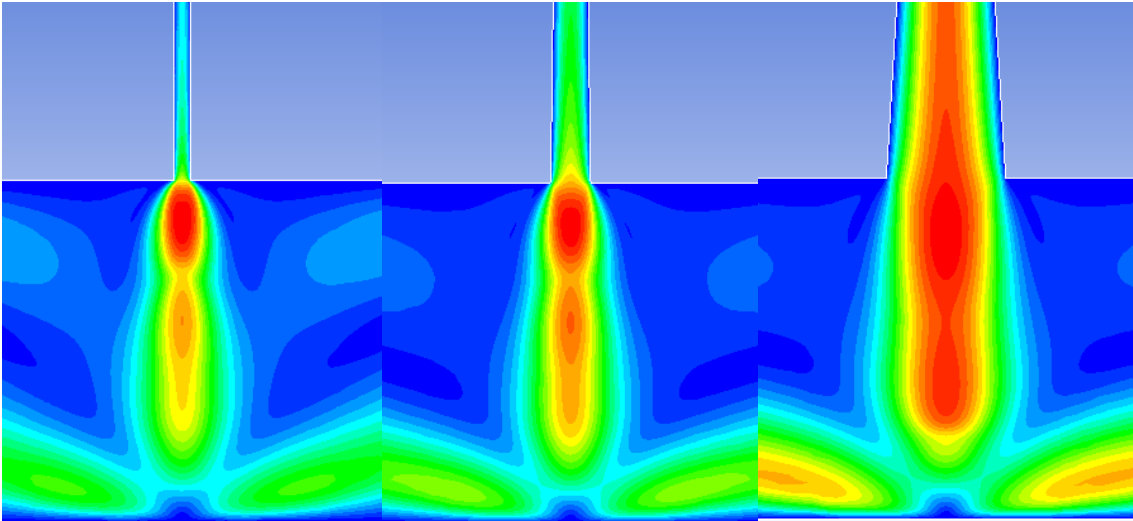


Figure 27 - Velocity Contour Plot, left: Baseline Nozzle; center: AMNR Nozzle; right: BLC Nozzle

The experiments for each of the nozzles were repeated with a change in the substrate stand-off distance from 10mm to 20mm. The results follow the same trend as the previous experiments. In the figure below, it is noted that the maximum velocity for the BLC nozzle is still less than the other two nozzles. However, as will be shown in the next section, the NC velocities are substantially greater for the BLC nozzle than for the other two nozzles.

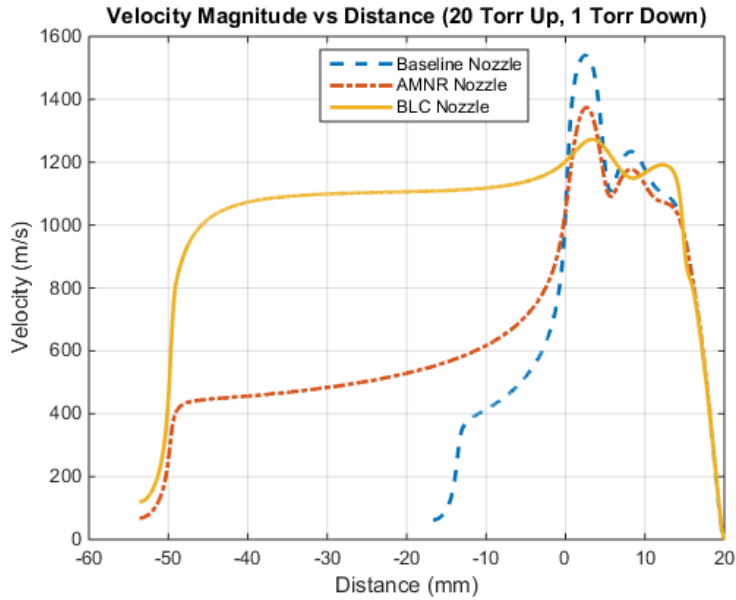


Figure 28 - Carrier Gas Velocity Magnitude along Centerline of Nozzle

Similar to the results above for a 10mm stand-off distance, the figure above depicts the maximum velocity magnitude aft of the exit plane (0 mm) of the BLC nozzle being less than the baseline nozzle and the AMNR nozzle. However, once again the carrier gas velocity is much greater within the BLC nozzle than the other two nozzles.

5.3 Nanoparticle Behavior (10mm stand-off)

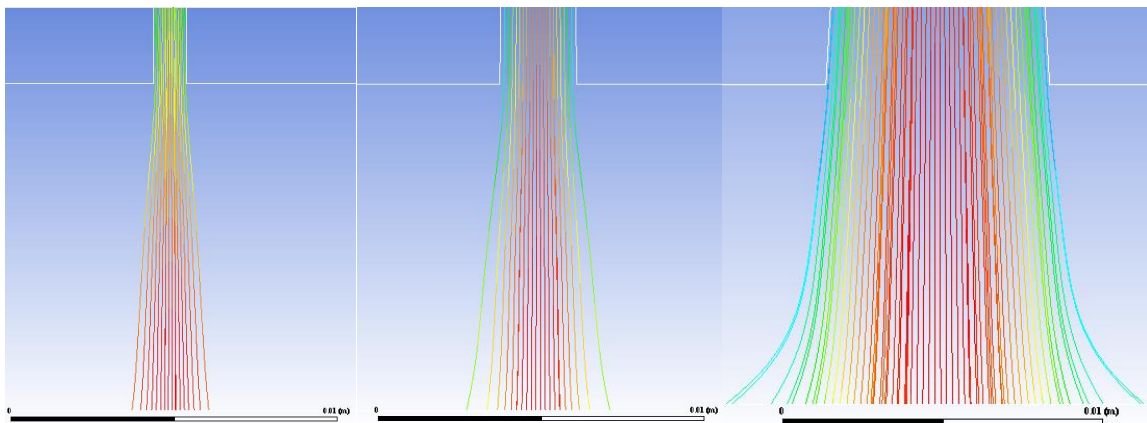


Figure 29 – Particle Streamlines, left: Baseline Nozzle; center: AMNR Nozzle; right: BLC Nozzle

The figure above illustrates particle streamlines for each of the three studied nozzles. It is noteworthy that the span-wise width of the NC flow associated with the baseline nozzle (left) at the substrate is over twice the nozzle exit width of the actual baseline nozzle. This expansion of the NC flow occurs because the carrier gas rapidly expands in the span-wise direction as it exits the baseline nozzle. In contrast, the carrier gas in the BLC nozzle has expanded to a pressure that is substantially equal to the deposition chamber pressure at the exit plane of the BLC nozzle.

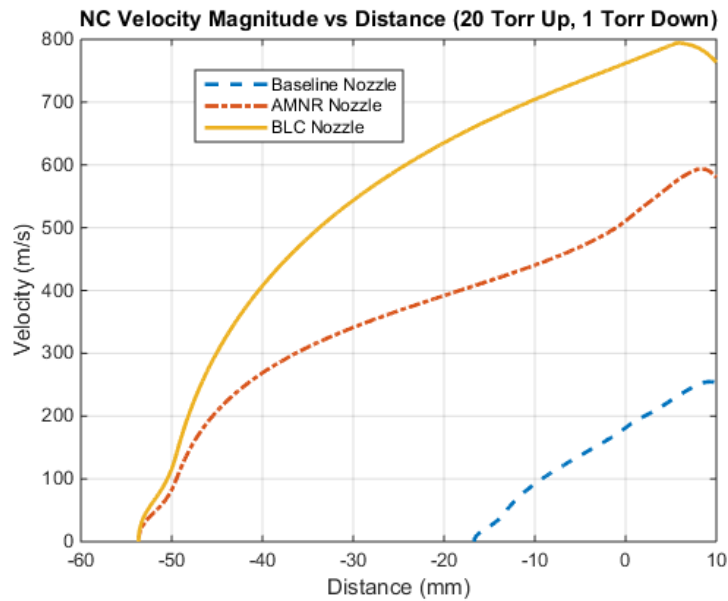


Figure 30 – NC Velocity Along Centerline of Nozzle

Although the maximum velocity magnitude for the BLC nozzle is minimal in comparison to the other two nozzles, the above figure clearly illustrates the advantage of the BLC nozzle. Because the carrier gas accelerates in the nozzle, the NCs are given time to accelerate in the nozzle with the carrier gas instead of trying to accelerate over a short distance after leaving the nozzle.

5.4 Nanoparticle Behavior (20mm stand-off)

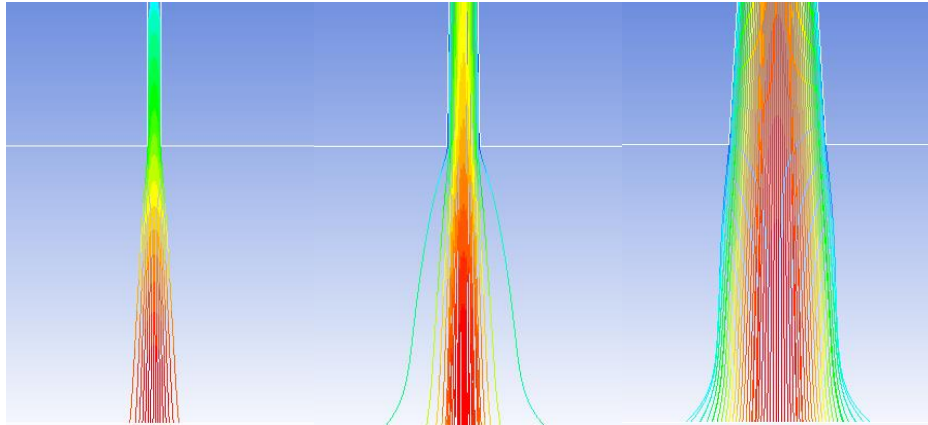


Figure 31 - Particle Streamlines, left: Baseline Nozzle; center: AMNR Nozzle; right: BLC Nozzle

The figure above illustrates the particle streamlines for each of the three studied nozzles with a stand-off distance of 20mm. The center figure depicts particles near the wall of the nozzle being caught in the boundary layer and dispersed in the span-wise direction away from the “core” particle flow. This is an example of the negative effects of span-wise expansion of the carrier gas due to an under-expanded nozzle.

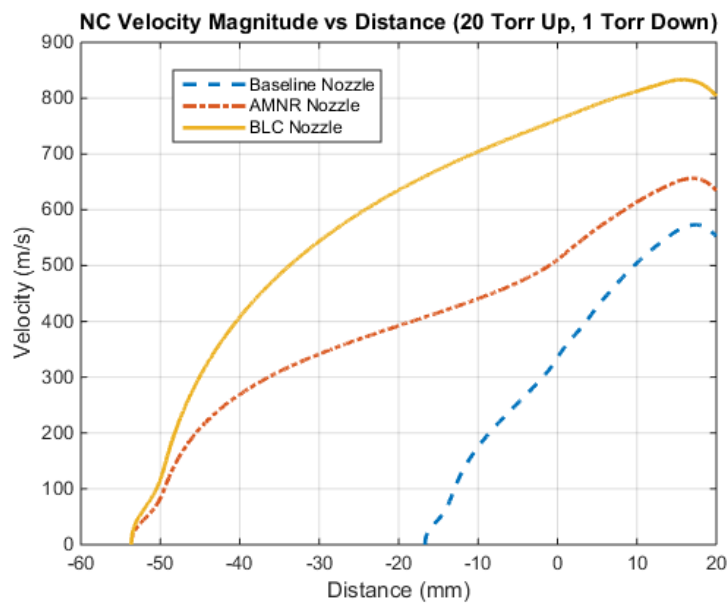


Figure 32 - NC Velocity Along Centerline of Nozzle

The table below shows that, for a 10mm stand-off, the BLC nozzle provides a 131% increase in particle velocity when compared to the AMNR nozzle and a 302% increase in particle velocity when compared to the baseline nozzle. For a 20mm stand-off, the BLC nozzle provides a 127% increase in particle velocity when compared to the AMNR nozzle and a 146% increase in particle velocity when compared to the baseline nozzle.

Table 3 – NC Impact Velocities

Nozzle Type	Substrate Stand-off (mm)	NC Impact Velocity (m/s)
Baseline	10	253
	20	552
AMNR	10	580
	20	634
BLC	10	764
	20	804

As a result of the increased NC impact velocities achieved by the BLC nozzle, the BLC nozzle is likely more suitable for use in depositing thin films for semiconductor devices which require dense films in which charge carriers can pass between neighboring nanoparticles.

6 FUTURE WORK

In this work various nozzle designs for an AD tool were investigated. ANSYS Fluent was utilized to accomplish this goal. A significant portion of the initial effort in this project was dedicated to learning how to navigate through the various tools that ANSYS Fluent provides, including nozzle design, mesh generation, setup, and post-processing. The results disclosed herein are promising that for a given pressure, the BLC nozzle provides significant advantages over traditional AMNR nozzles which don't account for effects of viscosity which dominate carrier gas flow under the pressure conditions utilized in AD methods. As a result of the BLC nozzle, higher NC velocities were attained. Thus, the BLC nozzle may be more suitable for use in semiconductor devices which require dense films in which charge carriers can pass between neighboring nanoparticles

While the BLC nozzle is promising, future work will involve depositing NCs onto a substrate in order to better understand the impact of the BLC nozzle on film density. The density and/or porosity will be measured using Rutherford Backscattering and ellipsometry.

WORKS CITED

- [1] M. G. Panthani and B. A. Korgel, "Nanocrystals for Electronics," *Annual Reviews*, vol. 3, pp. 287-311, 2012.
- [2] J. M. Luther, M. Law, M. C. Beard, Q. Song, M. O. Reese, R. J. Ellingson and A. J. Nozik, "Schottky Solar Cells Based on Colloidal Nanocrystal Films," *The American Chemical Society*, vol. 8, pp. 3488-3492, 2008.
- [3] Q. Dai, C. E. Duty and M. Z. Hu, "Semiconductor-Nanocrystals-Based White Light-Emitting Diodes," *Small (Weinheim an der Bergstrasse, Germany)*, vol. 6, no. 15, pp. 1577-1588, 2010.
- [4] A. H. Ip, S. M. Thon, S. Hoogland, O. Voznyy, D. Zhitomirsky, R. Debnath, L. Levina, L. R. Rollny, G. H. Carey, A. Fischer, K. W. Kemp, I. J. Kramer, Z. Ning, A. J. Labelle, K. W. Chou, A. Amassian and E. H. Sargent, "Hybrid passivated colloidal quantum dot solids," *Nature nanotechnology*, vol. 7, no. 9, pp. 577-582, 2012.
- [5] I. Kim, "LiNi_{0.4}Co_{0.3}Mn_{0.3}O₂ thin film electrode by aerosol," *Nanoscale Research Letters*, vol. 7, no. 64, 2012.
- [6] F. Hetsch, N. Zhao, S. V. Kershaw and A. L. Rogach, "Quantum dot field effect transistors," *Materials Today*, vol. 16, no. 9, pp. 312-325, 2013.
- [7] M. Schnabel, C. Weiss, P. Loper, P. R. Wilshaw and S. Janz, "Self-assembled silicon nanocrystal arrays for photovoltaics," *Physica status solidi. A, Applications and materials science*, vol. 212, no. 8, pp. 1649-1661, 2015.
- [8] D. Hanft, J. Exner, M. Schubert, T. Stocker, P. Fuierer and R. Moos, "An Overview of the Aerosol Deposition Method: Process," *Journal of Ceramic Science and Technology*, vol. 06, no. 03, pp. 147-182, 2015.
- [9] A. P. Alivisatos, "Perspectives on the Physical Chemistry of Semiconductor Nanocrystals," *The Journal of Physical Chemistry*, vol. 100, no. 31, p. 13226-13239, 1996.
- [10] C. B. Murray and C. R. Kagan, "Synthesis and Characterization of Monodisperse Nanocrystals and Close-Packed Nanocrystal Assemblies," *Annual Review of Materials Science*, vol. 30, pp. 545-610, 2000.

- [11] D. Vanmaekelbergh and P. Liljeroth, "Electron-conducting quantum dot solids: novel materials based on colloidal semiconductor nanocrystals," *Chemical Society Reviews*, vol. 34, no. 4, pp. 299-312, 2005.
- [12] D. J. Norris, A. L. Efros and S. C. Erwin, "Doped Nanocrystals," *Science*, vol. 319, no. 5871, pp. 1776-1779, 2008.
- [13] D. V. Talapin, J. Lee, M. V. Kovalenko and E. V. Shevchenko, "Prospects of Colloidal Nanocrystals for Electronic and Optoelectronic Applications," *The American Chemical Society*, vol. 110, no. 1, pp. 389-458, 2010.
- [14] C. B. Murray, D. J. Norris and M. G. Bawendi, "Synthesis and characterization of nearly monodisperse CdE (E = sulfur, selenium, tellurium) semiconductor nanocrystallites," *Journal of the American Chemical Society*, vol. 115, p. 8706, 1993.
- [15] O. I. Micic, J. R. Sprague, C. J. Curtis, K. M. Jones, J. L. Machol, A. J. Nozik, H. Giessen, B. Fluegel, G. Mohs and N. Peyghambarian, "Synthesis and Characterization of InP, GaP, and GaInP₂ Quantum Dots," *The Journal of Physical Chemistry*, vol. 99, pp. 7754-7759, 1995.
- [16] M. A. Hines and P. Guyot-Sionnest, "Bright UV-Blue Luminescent Colloidal ZnSe Nanocrystals," *The Journal of Physical Chemistry*, vol. 102, pp. 3655-3657, 1998.
- [17] O. I. Micic, S. P. Ahrenkiel, D. Bertram and A. Nozik, "Synthesis, structure, and optical properties of colloidal GaN quantum dots," *Applied Physics Letter*, vol. 75, no. 4, 1999.
- [18] C. B. Murray, S. H. Sun, W. Gaschler, H. Doyle, T. A. Betley and C. R. Kagan, "Colloidal synthesis of nanocrystals and nanocrystal superlattices," *Journal of Research and Development*, vol. 45, no. 1, pp. 47-56, 2001.
- [19] J. E. Murphey, M. C. Beard, A. G. Norman, S. P. Ahrenkiel, J. C. Johnson, P. Yu, O. I. Micic, R. J. Ellingston and A. J. Nozik, "PbTe Colloidal Nanocrystals: Synthesis, Characterization, and Multiple Exciton Generation," *Journal of the American Chemical Society*, vol. 128, pp. 3241-3247, 2006.
- [20] Biolin Scientific, "Fabricating Highly Organized Nanoparticle Thin Films," "<https://studylib.net/doc/18128168/fabricating-highly-organized-nanoparticle-thin-films>".
- [21] R. N. Pereira, J. Coutinho, S. Neisar, T. A. Oliveira, W. Aigner, H. Wiggers, M. J. Rayson, P. R. Briddon, M. S. Brandt and M. Stutzmann, "Resonant Electronic

Coupling Enabled by Small Molecules in," *American Chemical Society*, vol. 14, pp. 3817-3826, 2014.

- [22] P. Guyot-Sionnest, "Electrical Transport in Colloidal Quantum Dot Films," *The Journal of Physical Chemistry Letters*, vol. 3, pp. 1169-1175, 2012.
- [23] B. Moore, E. Asadi and G. Lewis, "Deposition Methods for Microstructured and Nanostructured Coatings on Metallic Bone Implants: A Review," *Advances in Materials Science and Engineering*, vol. 2017, 2017.
- [24] A. Moridi, S. M. Hassani-Gangaraj, M. Guagliano and M. Dao, "Cold spray coating: review of material systems," *Institute of Materials, Minerals and Mining*, vol. 36, no. 6, 2013.
- [25] Z. C. Holman and U. R. Kortshagen, "A flexible method for depositing dense nanocrystal thin films: impact of germanium," *Nanotechnology*, vol. 21, no. 33, 2010.
- [26] F. Cao, H. Park, G. Bae, J. Heo and C. Lee, "Microstructure Evolution of Titanium Nitride Film during Vacuum Kinetic Spraying," *Journal of the American Ceramic Society*, vol. 96, no. 1, pp. 40-43, 2013.
- [27] J. Kwon, H. Park, I. Lee and C. Lee, "Effect of gas flow rate on deposition behavior of Fe-based amorphous alloys in vacuum kinetic spray process," *Surface & Coatings Technology*, vol. 259, pp. 585-593, 2014.
- [28] J. Akedo, "Aerosol Deposition Method for Fabrication of Nano Crystal Ceramic Layer," *Mater. Sci. Forum*, pp. 449-452, 2004.
- [29] J. Akedo, "Aerosol Deposition of Ceramic Thick Films at Room Temperature:," *J. Am. Ceram. Soc.*, vol. 89, no. 6, pp. 1834-1839, 2006.
- [30] S. M. Nam, N. Mori, H. Kakemoto, S. Wada, J. Akedo and T. Tsurumi, "Alumina thick films as integral substrate using aerosol deposition method," *Japanese Journal of Applied Physics*, vol. 43, pp. 5414-5418, 2004.
- [31] U. R. Kortshagen, R. M. Sankaran, R. N. Pereira, S. L. Girshick, J. J. Wu and E. S. Aydil, "Nonthermal Plasma Synthesis of Nanocrystals: Fundamental Principles, Materials, and Applications," *Chemical Reviews*, vol. 116, pp. 11061-11127, 2016.
- [32] U. Kortshagen, "Nonthermal plasma synthesis of semiconductor nanocrystals," *J Phys D Appl Phys*, vol. 42, no. 11, 2009.

- [33] I. Dogan and van de Sanden MCM, "Gas-phase plasma synthesis of free-standing silicon nanoparticles for future energy applications," *Plasma Process Polym*, vol. 13, no. 1, pp. 19-53, 2015.
- [34] J. Godet, F. A. E. Nabi, S. Brochard and L. Pizzagalli, "Surface effects on the mechanical behavior of silicon nanowires: Consequence on the brittle to ductile transition at low scale and low temperature," *Phys. Status Solidi*, vol. 212, no. 8, pp. 1643-1648, 2015.
- [35] J. Rabier, A. Montagne, J. M. Wheeler, J. L. Demenet, J. Michler and R. Ghisleni, "Silicon micropillars: high stress plasticity," *Phys. Status Solidi*, vol. 10, no. 1, pp. 11-15, 2013.
- [36] F. Ostlund, K. Rzepiejewska-Malyska, K. Leifer, L. M. Hale, Y. Tang, R. Ballarini, W. W. Gerberich and J. Michler, "Brittle-to-Ductile Transition in Uniaxial Compression of Silicon Pillars at Room Temperature," *Advanced Functional Materials*, vol. 19, pp. 2439-2444, 2009.
- [37] ANSYS FLUENT 12.0/12.1 Documentation, ANSYS Inc., 2009.
- [38] J. D. Anderson, *Modern Compressible Flow : with Historical Perspective* 3rd Ed., New York: McGraw-Hill, 2003.
- [39] R. Bhaskaran and L. Collins, "Introduction to CFD Basics," <http://dragonfly.tam.cornell.edu/teaching/mae5230-cfd-intro-notes.pdf>.
- [40] P. Firth, (2015), *Substrate-Independent Nanomaterial Deposition Via Hypersonic Impaction*, (Masters Dissertation).
- [41] J.-B. M. Mbuyamba, (2013) *Calculation and Design of Supersonic Nozzles for Cold Gas Dynamic Spraying Using Matlab and Ansys Fluent*, (Masters Dissertation).
- [42] P. G. Blocker, (1995) *A Method of Characteristics Nozzle Design and Analysis Code with Improved Throat Modeling*, (Masters Dissertation).
- [43] B. R. Munson, T. H. Okiishi, W. W. Huebsch and A. P. Rothmayer, *Fundamentals of Fluid Mechanics: 7th Ed.*, Hoboken: John Wiley and Sons, Inc., 2013.
- [44] T. Benson, (2014) NASA: Reynolds Number [Online]., <https://www.grc.nasa.gov/www/BGH/reynolds.html>.
- [45] HyperPhysics, "Refinement of Mean Free Path," <http://hyperphysics.phy-astr.gsu.edu/hbase/Kinetic/menfre.html>.

- [46] ANSYS Fluent User's Guide: Release 15.0, ANSYS Inc., 2013.
- [47] D. L. Gilmore, R. C. Dykhuizen, R. A. Neiser, T. J. Roemer and M. F. Smith, "Particle Velocity and Deposition Efficiency in the Cold Spray Process," Sandi National Laboratories, Albuquerque, 1998.
- [48] D. K. Kim, Y. Lai, B. T. Diroll, C. B. Murray and C. R. Kagan, "Flexible and low-voltage integrated circuits constructed from high-performance nanocrystal transistors," *Nature communications*, vol. 3, p. 1216, 2012.
- [49] J.-J. Choi, K.-S. Cho, J.-H. Choi, J. Ryu, B.-D. Hahn, W.-H. Yoon, J.-W. Kim, C.-W. Ahn, J. Yun and D.-S. Park, "Low temperature preparation and characterization of LSGMC based IT-SOFC cell by aerosol deposition," *Journal of the European Ceramic Society*, vol. 32, no. 1, pp. 115-121, 2012.
- [50] "Brittle-to-Ductile Transition in Uniaxial Compression of Silicon Pillars at Room Temperature," *Advanced Functional Materials*, vol. 19, pp. 2439-2444, 2009.